# Mössbauer and Electrochemical Investigations of Carbon-Rich $Fe_{1-x}C_x$ Films

Xiuyun Zhao[a,b,c], R. J. Sanderson[a,c], L. MacEachern[a,b,c], R. A. Dunlap[a,c,d], M. N. Obrovac[a,b,c]*

[a] Department of Physics and Atmospheric Science, Dalhousie University, Halifax, Nova Scotia B3H 4R2, Canada

[b] Department of Chemistry, Dalhousie University, Halifax, Nova Scotia B3H 4R2,Canada

[c] Institute for Research in Materials, Dalhousie University, Halifax, Nova Scotia B3H 4R2, Canada

[d] College of Sustainability, Dalhousie University, Halifax, Nova Scotia B3H 4R2, Canada

*Corresponding author.

Email: mnobrovac@dal.ca (M.N. Obrovac)

## Abstract

A thin film binary library of carbon-rich $Fe_{1-x}C_x$ ($0.47 \leq x \leq 0.97$) alloys was prepared by combinatorial sputtering of carbon and iron. The sputtered library was characterized by X-ray diffraction (XRD) and room temperature $^{57}Fe$ Mössbauer effect spectroscopy to determine its microstructure. XRD results show that the $Fe_{1-x}C_x$ film is amorphous in the whole composition range of the library. For $0.52 \leq x \leq 0.59$, a hyperfine field distribution and a quadrupole splitting distribution as obtained from Mössbauer spectra indicate the presence of a ferromagnetic phase and a paramagnetic phase in this regime. With increasing of carbon content, for $0.61 \leq x \leq 0.97$, the sextet disappears and two paramagnetic doublets splitting appear suggesting two different Fe sites. The electrochemical performance of the $Fe_{1-x}C_x$ film was investigated in lithium cells and

the presence of Fe was found to increase the reversible capacity per mass of carbon over that of a pure carbon electrode.

*Keywords*: Mossbauer spectroscopy; lithium batteries; carbon-rich Fe-C alloy; sputtering

## 1. Introduction

The Fe-C binary alloy, as the basis of a number of steels and alloys, is interesting from both academic and industrial perspectives. Hence, large amounts of research have been performed to understand the metallographic structure and mechanical properties. Mössbauer effect spectroscopy is more sensitive to local atomic structure than X-ray diffraction (XRD) and is a unique tool that can be used to identify amorphous or nanocrystalline Fe-C alloy materials [1]. Bauer-Grosse and Le Caer studied the structure of sputtered amorphous $Fe_{1-x}C_x$ ($0.19 \leq x \leq 0.49$) films and discussed the effect of heat treatment on the formation of some carbides by Mössbauer spectroscopy analysis [2-5]. Cusenza et al. deposited $Fe_{1-x}C_x$ ($x = 0.10$, 0.20, 0.40, and 0.50) films and studied their structures using Mössbauer spectroscopy [6]. $Fe_{1-x}C_x$ ($x \leq 0.50$) powders prepared by mechanical alloying have also been studied by Mössbauer spectroscopy [7-9]. However, these reports are generally limited to relatively low carbon concentrations, with $x \leq 0.50$ in $Fe_{1-x}C_x$ alloys. Fewer studies have examined high carbon Fe-C alloys. Tanaka et al. ball milled $Fe_{1-x}C_x$ ($x = 0.17$-0.90) powders and showed the Mössbauer analysis of alloys with carbon contents of $x = 0.25$, 0.60, and 0.90 [10]. In addition, Al-Maghrabi et al. reported Mössbauer effect studies of sputtered $Fe_{1-x}C_x$ ($0.35 \leq x \leq 0.75$) films [11]. The systematic investigation of

carbon-rich $Fe_{1-x}C_x$ alloys is desirable in order to obtain a detailed understanding of the composition dependence of their structure and Mössbauer effect parameters.

Amorphous or nanocrystalline alloys comprising free carbon are potential negative electrode candidates for lithium-ion batteries due to their high volumetric capacity compared to commercial graphite. Dahn et al. prepared Sn-Co-C alloys by ball milling and combinatorial sputtering. These alloys were found to comprise a Sn-Co alloy phase and an amorphous carbon phase [12]. Purcell et al. sputtered C-Zn films comprising nanocrystalline Zn and amorphous carbon [13]. In these alloys it was found that 0.5 Li reacted per carbon, corresponding to a capacity of 1116 mAh/g or about 1360 Ah/L. This is about twice the volumetric capacity of graphite. In contrast, both Fathi et al. [14] and Subramanian et al. [15] found that pure sputtered amorphous carbon film has a reversible capacity of about 800 mAh/g, which is lower than that of amorphous carbon in the Sn-Co-C or C-Zn alloys. This makes it interesting to investigate the effects of metals on the electrochemistry of amorphous carbon in alloys.

The inclusion of Fe has been found to improve the electrochemical performance of carbon electrodes [16-18]. Su et al. [16,17] and Zhao et al. [18] investigated hydrogen-containing carbons comprising Fe or $Fe_3C$ made by a solvent thermal process or a polymer-pyrolysis method. However, to the best of our knowledge, there has been no systematic study of the effects of Fe content on the electrochemistry of carbon-rich Fe-C binary alloys in nonaqueous lithium cells.

The purpose of the present work is to investigate the micro- or nanostructure and electrochemistry in nonaqueous lithium cells of a carbon-rich Fe-C thin film library produced by combinatorial sputtering. X-ray diffraction (XRD), Mössbauer effect spectroscopy and electron microprobe analysis were be performed to characterize the library's structure and composition.

The Mössbauer parameters of Fe-C films as a function of Fe concentration are reported and the electrochemical properties of the library are described.

## 2. Experimental

A binary combinatorial library for the carbon-rich $Fe_{1-x}C_x$ system was produced using a Corona Vacuum Coater model V3-T multi-target sputtering system, which has been previously described [19]. Two carbon sputtering targets (50.8 mm diameter, 6.35 mm thick, and 99.999% pure) obtained from Kurt J. Lesker Co. Clairton, PA, were used with "constant" masks. One Fe sputtering target (a 50-mm-diameter disk cut from a grade 1008 low-C steel) was used with a "linear out" mask. All targets were mounted on 0.318 cm thick copper backing plates using Silver Tech PT-1 silver epoxy from Williams Advanced Materials. The distances between the masks and the substrates were kept small (about 1 mm) in order to control the sputtering flux. A base pressure of $3.8 \times 10^{-7}$ Torr was achieved before deposition and moisture was eliminated from the chamber using a Polycold PFC-400 cryopump. The chamber pressure was maintained at 1.0 mTorr of argon gas during deposition. The angular velocity of the sputtering table was 15 rpm to ensure atomic level mixing. Carbon was deposited using two targets with direct current power supplies at 145 W and 147 W, respectively. Fe was sputtered using a dc power supply at 39 W. Continuous films on the 76 mm wide sputter track were deposited on a variety of substrates: a linear array of 1.27 cm diameter Cu foil weighing disks for mass determination and electrochemical testing, two 77 mm long silicon (100) wafers for electron microprobe studies and XRD measurements, 16 Kapton strips, each approximately 25 mm $\times$ 100 mm, for Mössbauer effect studies.

A Sartorius microbalance (0.1 μg precision) was used to weigh the Cu foil disks before and after sputtering to determine the mass per unit area deposited as a function of position on the library. These weighing disks were also used as electrodes for constructing coin cells.

The $Fe_{1-x}C_x$ film library composition was determined using a JEOL-8200 Superprobe electron microprobe equipped with a translation stage, using wavelength dispersive spectroscopy (WDS). XRD measurements were performed using a Bruker D-8 Discover diffractometer equipped with a Vantec-2000 area detector and a Cu target X-ray tube.

Room temperature $^{57}$Fe Mössbauer effect spectra were collected using a resonant gamma-ray system spectrometer (Model W302 from SEE Co.) equipped with a $Rh^{57}$ Co source. Sixteen layers of $Fe_{1-x}C_x$ film deposited onto Kapton strips were compositionally aligned and attached together to be used as the absorber. The spectrometer was calibrated relative to room temperature α-Fe. Spectra of different compositions were obtained by moving the sample in front of a 4.5 mm × 25 mm lead aperture. The range of film compositions measured was $0.52 \leq x \leq 0.97$ in $Fe_{1-x}C_x$. Data acquisition times at each position were typically 24 h. The Mössbauer spectra were fitted using the Recoil program [20].

2325 coin cells were used for electrochemical testing of the $Fe_{1-x}C_x$ film library. Li metal (Aldrich, 99.9%) was used as the counter/reference electrode. Two layers of Celgard 2300 microporous films were used as separators (available from 3M Company). A solution of 1 M $LiPF_6$ in ethylene carbonate / diethyl carbonate / fluoroethylene carbonate 30/60/10 by volume was used as electrolyte. Cell assembly was conducted in an argon-filled glovebox. Electrochemical tests were performed using a Maccor Series 4000 Automated Test System. Cells were discharged and charged between 0.005 V to 2.0 V at a C/20 rate with a trickle of C/40 at 30.0 ± 0.1 °C, where C is calculated assuming that only carbon is active (0.5 lithium per

carbon) and that Fe is inactive to lithium. This corresponds to a theoretical gravimetric capacity range of 210 mAh/g to 975 mAh/g in the $0.52 \leq x \leq 0.97$ in $Fe_{1-x}C_x$ composition range studied.

## 3. Results and Discussion

### *3.1 Compositional and structural analysis*

Fig. 1a-c illustrates the composition analysis method for the Fe-C combinatorial film. The "constant" mask placed over the carbon target ensures that the moles of carbon deposited per unit area is a constant value, A, across the 76 mm library. The "linear out" mask ensures that the moles of Fe deposited per unit area increases linearly from zero to a maximum value, B, across the library. The theoretical compositions were calculated from the constant carbon mass per unit area and the linear variation in the Fe mass per unit area as:

$$\text{mass} / \text{area} = \{(12.01 \text{ g/mol})A + (55.85 \text{ g/mol})[y/(76 \text{ mm})]B\}, \quad (1)$$

where the constants 12.01 g/mol and 55.85 g/mol are the molar masses of C and Fe, respectively and A and B are in units of mol/cm$^2$. The parameter, y (in mm), measures the position along the library with y = 0 at the C-rich end and y = 76 mm at the Fe-rich end of the library. Fig. 1a shows the number of moles of C and Fe deposited per unit area plotted as position along the library as obtained by a least squares fit for the parameters A and B to WDS composition measurements.

Fig. 1b shows the calculated mass based on the microprobe measurements shown in Fig. 1a, and the measured mass of the sputtered film. There is good agreement between the two sets

of data. Fig. 1c shows the WDS measurements and the fit in Fig. 1a plotted with respect to the mole fractions of Fe and C as a function of position on the film.

Fig. 2 shows the XRD patterns collected across the composition range of the $Fe_{1-x}C_x$ film library. The profiles from bottom to top correspond to positions spaced about 4 mm apart in the direction along the 76 mm library from the carbon-rich to Fe-rich edge. These patterns are typical for an amorphous or nanostructured material and no sharp peaks indicative of any crystalline phases can be observed. As the Fe concentration increased across the library, a broad peak around 44° is observed which can be attributed to an increase in regions with Fe–Fe correlated near neighbors in a nanostructured phase. This result is in good agreement with a previous report on sputtered $Fe_{1-x}C_x$ films with $0.35 \leq x \leq 0.75$ [11].

### *3.2 Mössbauer studies*

Fig. 3 shows room temperature $^{57}$Fe Mössbauer spectra of the sputtered $Fe_{1-x}C_x$ film for a series of compositions. Voigt-based functions (VBF) were used to fit these Mössbauer spectra. The spectra fall into two regions as follows: when the carbon content is between x = 0.52 and 0.59, the spectra are fit to a quadrupole split doublet and a magnetically split sextet, as shown in Fig. 3a. For $0.61 \leq x \leq 0.97$ in Fig. 3b, the spectra show two quadrupole split doublets. Table 1 gives the fitted parameters deduced from the room temperature Mössbauer spectra in Fig. 3. The center shifts with respect to α-Fe for the sextets and doublets are plotted in Fig. 4a and b. For $0.52 \leq x \leq 0.59$, it is found that the center shift for the sextet increases from +0.206 to +0.225 mm/s, while the center shift for the doublet decreases from +0.253 to +0.228 mm/s and the quadrupole splitting of the doublet decreases from 0.801 to 0.733 mm/s with the decreasing of Fe content (see Table 1 and Fig. 4c). Fig. 4d shows the change in the internal magnetic field of the sextet in the Mössbauer spectra as a function of carbon content in $Fe_{1-x}C_x$ film library. When

carbon content is 52 at. %, the hyperfine field is around 11.2 T. As the carbon content increases to 59 at. %, the hyperfine field is reduced to 9.0 T. For $0.61 \leq x \leq 0.97$, the mean center shift for the two doublets increases from +0.224 to +0.311 mm/s and the mean quadrupole splitting of the doublet increases from 0.741 to 1.017 mm/s with the decreasing of Fe content (see Table 1). The parameters obtained from these Mössbauer spectra are consistent with the previously reported results [11].

Bauer-Gross et al. [10] and Al-Maghrabi et al. [11] have used the semi-empirical model of Miedema and van der Woude [21] to account for the concentration dependence of mean center shift in sputtered Fe-C films. The calculated slope $d\bar{\delta}/dX_s$ ($\bar{\delta}$ is a mean center shift and $X_s$ is a surface concentration defined in the Miedema-van der Woude model) is -0.50 mm/s based on the numerical values tabulated by Miedema et al. [22] and Hoving et al. [23] Based on the slope data from both Bauer-Gross et al. [10] and Al-Maghrabi et al. [11], a linear relationship between the mean center shift and the surface concentration can be found for the Fe-rich compositions, while the mean center shift remains fairly constant as the surface concentration decreases for the lower Fe compositions. For the Fe-rich linear region, Bauer-Gross et al. [10] have obtained a slope of -1.27 mm/s which is not consistent with the above model. Al-Maghrabi et al. [11] have obtained a slope of -0.45 mm/s for the high carbon region which is in good agreement with the above model. Here, based on the data from the present work, the mean center shift as a function of surface concentration is plotted in Fig. 5. For $X_s > 0.35$, the center shift is relatively constant with surface composition, in good agreement with the data from Al-Maghrabi et al. [11]; while for $X_s < 0.35$, with decreasing of surface concentration even to near $X_s = 0$, the center shift increases significantly. This increasing region can be fit to a linear relationship with a slope of -0.35 mm/s, indicating that the Miedema van der Woude model is applicable in the dilute $X_s = 0$ limit.

At the Fe edge of the library, the $Fe_{1-x}C_x$ ($0.52 \leq x \leq 0.59$) film includes both a ferromagnetic phase and a paramagnetic phase. The hyperfine field distribution of the magnetic component may be related to the nearest-neighbor environment of the Fe atoms. Compared to a hyperfine field of 33 T for α-Fe, the mean field value for the $Fe_{1-x}C_x$ film in this composition region, as shown in Table 1, can be attributed to Fe with carbon near neighbors. With the decreasing of Fe content, the center shift increases and the hyperfine magnetic field decreases, as shown in Table 1, indicating that the composition of the ferromagnetic phase is becoming less Fe rich. It is found that when x = 0.61, the magnetic splitting disappears, indicating that this composition corresponds to the room temperature magnetic percolation limit and alloys with high carbon concentrations do not show long range ferromagnetic order. For the composition of the paramagnetic phase, it is difficult to tell if it is becoming more or less Fe rich because both the total Fe in the sample and the Fe in the ferromagnetic phase are decreasing from x = 0.52 to x = 0.59. However, since the relative absorption increases from 44 % to 72 % for the paramagnetic phase while the overall Fe composition of the sample only decreases from 48 at % to 41 at %, as shown in Table 1, it is possible that the composition of the paramagnetic phase becomes more Fe rich as the overall composition becomes more carbon rich over this composition range. This is consistent with the center shift of the paramagnetic component which also becomes more Fe-like as the total Fe content decreases.

The quadrupole splitting results from asymmetric environments of the Fe atoms in the amorphous $Fe_{1-x}C_x$ film caused by a non-isotropic arrangement of Fe and C atoms around the Fe probe atom. A symmetric environment can be expected in the cases of very dilute Fe in carbon or a uniform 50/50 mixture of Fe and C. As the Fe content is decreased over the range of total composition from 1 - x = 0.48 to 1 - x = 0.41, the Fe content of the paramagnetic phase

increases, but remains less than the magnetic percolation limit of about 50 at. %. The quadrupole splitting of the doublet shown in Table 1 shows a decreasing trend from 0.801 to 0.733 mm/s, indicative of an increase in the symmetry of the Fe atomic environment. This is because the Fe content in the paramagnetic phase is mostly in the range that is near the uniform 50/50 mixture of Fe and C. This result is also consistent with a decreasing center shift and a composition that remains below the magnetic percolation limit. With increasing of carbon content, for $0.61 \leq x \leq 0.97$, the presence of two different quadrupole splittings suggests the presence of two distinct classes of Fe sites. In this region, some Fe atoms have more carbon atom neighbors, corresponding to the more positive center shift; while the other Fe atoms have less carbon atom neighbors, corresponding to the less positive center shift.

### *3.3 Electrochemical studies*

Fig. 6a and b show the potential versus specific capacity curves for the first one and a half cycles of eight selected compositions across the sputtered $Fe_{1-x}C_x$ library. The carbon content is indicated in each panel. In Fig. 6a, the specific capacity is calculated based on the total mass of $Fe_{1-x}C_x$ film. In order to better investigate the effect of Fe on the electrochemical performance of the carbon phase in the $Fe_{1-x}C_x$ films, the specific capacity is calculated based only on the mass of carbon in the film in Fig. 6b. The voltage curves have long sloping plateaus, and the plateaus become more sloped with decreasing of Fe content. Compared to the sputtered C-Zn films reported by Purcell et al. [13], a larger hysteresis can be found from the voltage curves of $Fe_{1-x}C_x$ films.

Fig. 7 shows the differential capacity of the cells shown in Fig. 6, calculated based on the mass of carbon or the first two cycles. During the first discharge all cells show peaks at about 1.5

V, 0.8 V, 0.7 V and excess capacity at lower voltage. We attribute these features to the formation of the SEI layer. These features grow as the Fe content is increased, which would increase the effective surface are per mass of carbon and may also increase the catalytic activity of the electrode towards electrolyte reduction per mass of carbon. After the initial cycle, these features disappear.

All of the differential capacity curves shown in Fig. 7 have a peak at about 0.8 V during charge that decreases in size as the iron content is increased and reduces in size after the first cycle. This peak is similar to the peak in differential capacity that is associated with the removal of lithium from hydrogen terminated carbons [24], however the hydrogen content in the sputtered $Fe_{1-x}C_x$ films investigated here is expected to be low. Similar observations have been made for disordered carbons made by ball milling [25]. Such carbons can contain edge carbons terminated by dangling bonds that may result in similar voltage curve features as hydrogen containing carbons.

Fig. 8 shows the first reversible capacity as a function of Fe content (1-x) in the $Fe_{1-x}C_x$ films as calculated based on total film weight and the weight of the carbon in the film only. When the specific capacity is calculated based on the total mass of electrode, the reversible capacity decreases from 1035 mAh/g to 334 mAh/g with increasing of Fe content. This is to be expected, since as the Fe content increases one would expect the mass of the film to increase and perhaps some iron carbide may form, which would reduce the amount of active carbon present. Both these effects would tend to reduce the specific capacity of the films. However, when the specific capacity is calculated based on the mass of carbon, the capacity is almost constant at $1600 \pm 50$ mAh/g for $1\text{-}x < 0.23$; and then increases to about $1875 \pm 100$ mAh/g for $0.23 < 1\text{-}x < 0.48$. The carbon capacity decreases slightly for the highest Fe content film shown in Fig. 8.

However, because the carbon content at this composition is low, the error in the capacity calculated by this method will be higher than for the other compositions. This general trend indicates that the Fe added does not reduce the capacity of the carbon phase by the formation of inactive iron carbides in sputtered $Fe_{1-x}C_x$ film. In fact, the presence of Fe seems to increase the capacity of the carbon.

To explain why the carbon capacity in the $Fe_{1-x}C_x$ films is does not decrease with Fe content, we first consider the possibility of iron carbide formation. Such carbides are likely inactive, as mentioned above and therefore would tend to reduce the carbon capacity. The Mössbauer results, however, clearly show center shifts that are indicative of Fe probe atoms interacting with some carbon atoms. The center shifts, which in the paramagnetic alloys range from about +0.22 mm/s to +0.31 mm/s (Table 1), suggest Fe environments that are intermediate between all Fe neighbors (with a center shift of 0 mm/s) and an environment with all carbon neighbors (center shift near +0.5 mm/s).

The Mössbauer data and the electrochemical results can be justified if Fe atoms form relatively small clusters involving both Fe and C atoms such that the local environment around the Fe atoms contains both Fe and C atoms and these clusters are separated by regions of relatively pure carbon that remains active. As the average Fe content in the alloy is decreased the average number of Fe-Fe neighbors with in the Fe containing regions decreases and the average number of Fe-C neighbors increases, leading to a more positive center shift. Thus the Mössbauer results show trends that are consistent with the changing Fe/C ratio within inactive clusters, while the relatively constant capacity results from the presence of relatively unchanging active carbon regions.

The highest reversible carbon capacity in the $Fe_{1-x}C_x$ films is 1957 mAh/g, which occurs at 1-x = 0.39. This corresponds to 0.88 Li reacting per carbon, which is more than twice the capacity of pure carbon reported by Fathi et al. [14] and Subramanian et al. [15] and is much higher than has been reported for the carbon phase in Sn-Co-C and C-Zn alloys [12,13]. This reversible capacity is also much higher than has been reported for hard carbons, hydrogen containing carbons or other disordered carbon phases [26]. As such, we believe that this is the highest reversible lithiation capacity reported for a carbonaceous phase. This extra capacity can be seen to occur as broad reduction and oxidation peaks at about 0.75 V and 1.0 V, respectively, in the differential capacity curves shown in Fig. 7, which grow in size as the Fe content is increased. We speculate that this extra capacity may occur from Li insertion at the Fe-C grain boundaries, as has been observed in the grain boundaries of $SnMn_3C$ [27] or a reversible SEI forming/dissolution process catalyzed by Fe may occur during cycling, which also has been observed in C-Ni nanocomposites [28], and in conversion-type oxides [29].

A comparison of the first cycle irreversible capacity based on the total $Fe_{1-x}C_x$ film mass and the carbon mass only is illustrated in Fig. 9. The irreversible capacity decreases gradually with increasing of Fe content (as the electrode mass increases) when the capacity is based on the total $Fe_{1-x}C_x$ film mass. When the irreversible capacity is calculated based on the mass of carbon, the irreversible capacity increases significantly from 522 mAh/g to 1029 mAh/g for $0.09 < 1-x < 0.39$. The capacity then decreases to 767 mAh/g at 1-x = 0.48, although there may be significant error in the capacity at this composition, as mentioned above. The reason for the increase in irreversible capacity with Fe content could be attributed to the electrolyte decomposition at the electrode surface induced by Fe, as discussed above. Fig. 10 shows the initial coulombic efficiency (ICE) as a function of Fe content for the sputtered $Fe_{1-x}C_x$ electrodes. The ICE is about

70 ± 5% across the $Fe_{1-x}C_x$ library, which is a little lower than that of a pure carbon film [14, 15]. The relatively constant ICE with composition reflects that as the Fe content is increased, both the irreversible carbon capacity and reversible carbon capacity increase.

## 4. Conclusions

A binary carbon-rich $Fe_{1-x}C_x$ ($0.47 \leq x \leq 0.97$) thin film library was prepared by combinatorial magnetron sputtering. The $Fe_{1-x}C_x$ film was amorphous or nanostructured across the entire composition range, as determined by XRD. Mössbauer spectra show that for $0.52 \leq x \leq 0.59$, the presence of both a hyperfine field distribution and a quadrupole splitting distribution indicates mixed ferromagnetic and paramagnetic behavior. With increasing of carbon content, for $0.61 \leq x \leq 0.97$, the magnetic splitting disappears and two different quadrupole doublets appear indicating two distinctly different Fe sites. A minimum in the quadrupole splitting near the transition between ferromagnetic and paramagnetic behavior suggests a maximum in the degree of randomization of Fe and C in the structure.

The $Fe_{1-x}C_x$ ($0.47 \leq x \leq 0.97$) films were found to have capacities above 1500 mAh/(g carbon), which is the highest capacity we are aware of for a carbonaceous phase. A reversible SEI forming/dissolution process may occur during cycling, which has been suggested in an earlier study.

## 5. Acknowledgements

The authors acknowledge funding from NSERC and 3M Canada, Co. under the auspices of the Industrial Research Chair and Discovery Grant programs and for financial support from the Dalhousie Research in Energy Advanced Materials and Sustainability (DREAMS) program.

| | Sextet | | | Doublet(s) | | |
|---|---|---|---|---|---|---|
| x | Mean Center Shift (mm/s) | H (T) | Area (%) | Mean Center Shift (mm/s) | Mean Quadrupole Splitting (mm/s) | Area (%) |
| 0.52 | +0.206 | 11.2 | 56 | +0.253 | 0.801 | 44 |
| 0.53 | +0.211 | 11.0 | 58 | +0.249 | 0.763 | 42 |
| 0.55 | +0.213 | 10.6 | 53 | +0.245 | 0.789 | 47 |
| 0.56 | +0.214 | 10.2 | 49 | +0.247 | 0.758 | 51 |
| 0.58 | +0.220 | 9.6 | 54 | +0.239 | 0.795 | 46 |
| 0.59 | +0.225 | 9.0 | 28 | +0.228 | 0.733 | 72 |
| 0.61 | | | | +0.224 | 0.741 | |
| 0.64 | | | | +0.221 | 0.703 | |
| 0.67 | | | | +0.224 | 0.714 | |
| 0.71 | | | | +0.227 | 0.728 | |
| 0.76 | | | | +0.231 | 0.754 | |
| 0.80 | | | | +0.240 | 0.771 | |
| 0.85 | | | | +0.249 | 0.796 | |
| 0.89 | | | | +0.279 | 0.889 | |
| 0.93 | | | | +0.304 | 0.937 | |
| 0.97 | | | | +0.311 | 1.017 | |

**Table 1** Mean center shifts, hyperfine fields (H), quadrupole splittings, and relative site populations (areas) for the sextet and doublets used to fit the Mössbauer spectra of the $Fe_{1-x}C_x$ thin film library. Experimental uncertainties for velocities are typically ±0.005 mm/s, for hyperfine fields are ±0.1 T and for areas are ±1%.

FIGURE CAPTIONS

**Fig. 1.** Calculated and experimental compositions of the $Fe_{1-x}C_x$ thin film libraries; (a) calculated C and Fe moles per unit area defined by the "constant" and "linear out" sputtering masks, (b) calculated mass per unit area (based on the graph in (a)) showing agreement with the measured mass, and (c) compositions calculated from (a) and (b) showing agreement with the measured values from wavelength dispersive spectroscopy.

**Fig. 2.** XRD patterns collected at 20 different positions in the $Fe_{1-x}C_x$ film libraries. The Fe content increases from bottom to top as indicated by the legend at the right. (Dashed line: Fe JCPDS 00-006-0696)

**Fig. 3.** Room temperature $^{57}$Fe Mössbauer effect spectra of $Fe_{1-x}C_x$film library as a function of C content. (a) $0.50 \leq x \leq 0.56$, (b) $0.58 \leq x \leq 0.94$. The velocity scale is measured relative to room temperature α-Fe.

**Fig. 4.** (a) Center shifts for the sextet, (b) mean center shifts for the doublets, (c) mean quadrupole splittings for the doublets, and (d) hyperfine fields for the sextet as a function of carbon content in $Fe_{1-x}C_x$ thin film library.

**Fig. 5.** Mean center shift as a function of surface concentration ($X_s$) for the $Fe_{1-x}C_x$ thin film. The solid line corresponds to a linear fit to the data.

**Fig. 6.** Potential versus specific capacity curves for the first 1.5 cycles of six selected compositions across the $Fe_{1-x}C_x$ thin film. The carbon content is indicated in the top right of each panel. Capacity is calculated based on the total weight (a) and carbon weight (b), respectively, for each electrode.

**Fig. 7.** Differential capacity versus potential curves between 2.0 and 0.005 V for the 1$^{st}$ and 2$^{nd}$ cycles of six selected compositions across the $Fe_{1-x}C_x$ film. The carbon content is indicated in the top right of each panel. Capacity was calculated based on the carbon mass for each electrode.

**Fig. 8.** Reversible capacities as a function of Fe content (1-x) in the first cycle for six selected compositions of the $Fe_{1-x}C_x$ thin film electrode. The capacity is calculated based on the total $Fe_{1-x}C_x$ film weight and on the carbon weight, as indicated.

**Fig. 9.** Irreversible capacities as a function of Fe content (1-x) in the first cycle for six selected compositions of the $Fe_{1-x}C_x$ thin film electrode. The capacity is calculated based on the total $Fe_{1-x}C_x$ film weight and on the carbon weight, as indicated.

**Fig. 10.** Initial coulombic efficiency as a function of Fe content (1-x) for the $Fe_{1-x}C_x$ thin film electrode.

## References


[1] R.A. Dunlap, O. Mao, J.R. Dahn, Application of in situ Mössbauer effect methods for the study of electrochemical reactions in lithium-ion battery electrode materials, Phys Rev B 59 (1999) 3494.

[2] E. Bauer-Grosse, G. Le Caër, Crystallisation of amorphous $Fe_{1-x}C_x$ alloys ($0.30 \leq x \leq 0.32$) and chemical twinning, J Phys F: Met Phys 16 (1986) 399.

[3] E. Bauer-Grosse, G. Le Caër, Structural evolution of sputtered amorphous $Fe_{1-x}C_x$ films for $0.19 \leq x \leq 0.49$, Philos Mag B 56 (1987) 485.

[4] E. Bauer-Grosse, G. Le Caër, L. Fournes, Mössbauer study of amorphous and crystallized $Fe_{1-x}C_x$ alloys, Hyperf Interact 27 (1986) 297.

[5] G. Le Caër, E. Bauer-Grosse, Aperiodic carbides formed by crystallization of amorphous Fe-C alloys, Hyperf Interact 47 (1989) 55.

[6] S. Cusenza, M. Seibt, P. Schaaf, Deposition and properties of high-carbon iron films, Appl Surf Sci 254 (2007) 955.

[7] E.P. Yelsukov, G.A. Dorofeev, A.V. Zagainov, N.F. Vildanova, A.N. Maratkanova, Initial stage of mechanical alloying in the Fe-C system, Mater Sci Eng A 369 (2004) 16.

[8] V.M. Nadutov, B.N. Mordyuk, G.I. Prokopenko, I.S. Gavrilenko, Mössbauer and X-ray studies of Fe-powder mechanically alloyed with C using power ultrasonics, Ultrasonics 42 (2004) 47.

[9] G. Le Caër, P. Matteazzi, Mössbauer study of mechanosynthesized iron carbides, Hyperf Interact 66 (1991) 309.

[10] T. Tanaka, S. Nasu, K.N. Ishihara, P.H. Shingu, Mechanical alloying of the high carbon Fe-C system, J Less-Commom Metals 171 (1991) 237.

[11] M.A. Al-Maghrabi, R.J. Sanderson, R.A. Dunlap, Mössbauer effect studies of Fe-C combinatorially sputtered thin films, Philos Mag 93 (2013) 3278.

[12] J.R. Dahn, R.E. Mar, A. Abouzeid, Combinatorial study of $Sn_{1-x}Co_x$ ($0 < x < 0.6$) and $[Sn_{0.55}Co_{0.45}]_{1-y}C_y$ ($0 < y < 0.5$) alloy negative electrode materials for Li-Ion batteries, J Electrochem Soc 153 (2006) A361.

[13] M.I. Purcell, T.D. Hatchard, R.J. Sanderson, M.N. Obrovac, An investigation of the C-Zn system as lithium-ion battery anode materials, J Electrochem Soc 161 (2014) A643.

[14] R. Fathi, R.J. Sanderson, L.J. Lucas, J.R. Dahn, The electrochemical reaction of lithium with high-capacity dense sputtered carbon, Carbon 74 (2014) 249.

[15] V. Subramanian, T. Karabacakb, C. Masarapua, R. Tekic, T.M. Lud, B. Wei, Low hydrogen containing amorphous carbon films-growth and electrochemical properties as lithium battery anodes, J Power Sources 195 (2010) 2044.

[16] L. Su, Y. Zhong, Z. Zhou, Role of transition metal nanoparticles in the extra lithium storage capacity of transition metal oxides: a case study of hierarchical core-shell $Fe_3O_4$@C and Fe@C microspheres, J Mater Chem A 1 (2013) 15158.

[17] L. Su, Z. Zhou, P. Shen, Core-shell Fe@$Fe_3C$/C nanocomposites as anode materials for Li ion batteries, Electrochim Acta 87 (2013) 180.

[18] X. Zhao, D. Xia, J. Yue, S. Liu, In-situ generated nano-$Fe_3C$ embedded into nitrogen-doped carbon for high performance anode in lithium ion battery, Electrochim Acta 116 (2014) 292.

[19] J.R. Dahn, S. Trussler, T.D. Hatchard, A. Bonakdarpour, J.R. Mueller-Neuhaus, K.C. Hewitt, M. Fleischauer, Economical sputtering system to produce large-size composition-

spread libraries having linear and orthogonal stoichiometry variations, Chem Mater 14 (2002) 3519.

[20] K. Lagarec, D.G. Rancourt, Recoil: Mössbauer spectral analysis software for windows, http://www.isapps.ca/recoil/ (1998).

[21] A.R. Miedema, F. van der Woude, A cellular atomic model for the Mössbauer isomer shift of $^{197}$Au in alloys, Physica B 100 (1980) 145.

[22] A.R. Miedema, P.F. De Chatel, F.R. De Boer, Cohesion in alloys-fundamentals of a semi-empirical model, Physica B 100 (1980) 1.

[23] W. Hoving, P.M.L.O. Scholte, P. Dorenbos, G.A. Fokkema, E.A.G. Weits, F. van der Woude, I. Vincze, K.H.J. Buschow, Packing and chemical effects in amorphous Fe-Zr and Fe-B alloys, Phys Rev B 32 (1985) 8368.

[24] T. Zheng, W.R. McKinnon, J.R. Dahn, Hysteresis during lithium insertion in hydrogen-containing carbons, J Electrochem Soc 143 (1996) 2137.

[25] F. Salver-Disma, C. Lenain, B. Beaudoin, L. Aymard, J.M. Tarascon, Unique effect of mechanical milling on the lithium intercalation properties of different carbons, Solid State Ionics 98 (1997) 145.

[26] J.R. Dahn, T. Zheng, Y. Liu, J.S. Xue, Mechanisms for lithium insertion in carbonaceous materials, Science 270 (1995) 590.

[27] L.Y. Beaulieu, D. Larcher, R.A. Dunlap, J.R. Dahn, Reaction of Li with grain-boundary atoms in nanostructured compounds, J Electrochem Soc 147 (2000) 3206.

[28] L. Su, Z. Zhou, P. Shen, Ni/C hierarchical nanostructures with Ni nanoparticles highly dispersed in N-containing carbon nanosheets: origin of Li storage capacity, J Phys Chem C 116 (2012) 23974.

[29] M. Dolle, P. Poizot, L. Dupont, J.M. Tarascon, Experimental evidnce for electrolyte involvement in the reversivle reacitvity of CoO toward compounds at low potentia, Electrochem. Solid-State Lett. 5 (2002) A18.

Figure 1

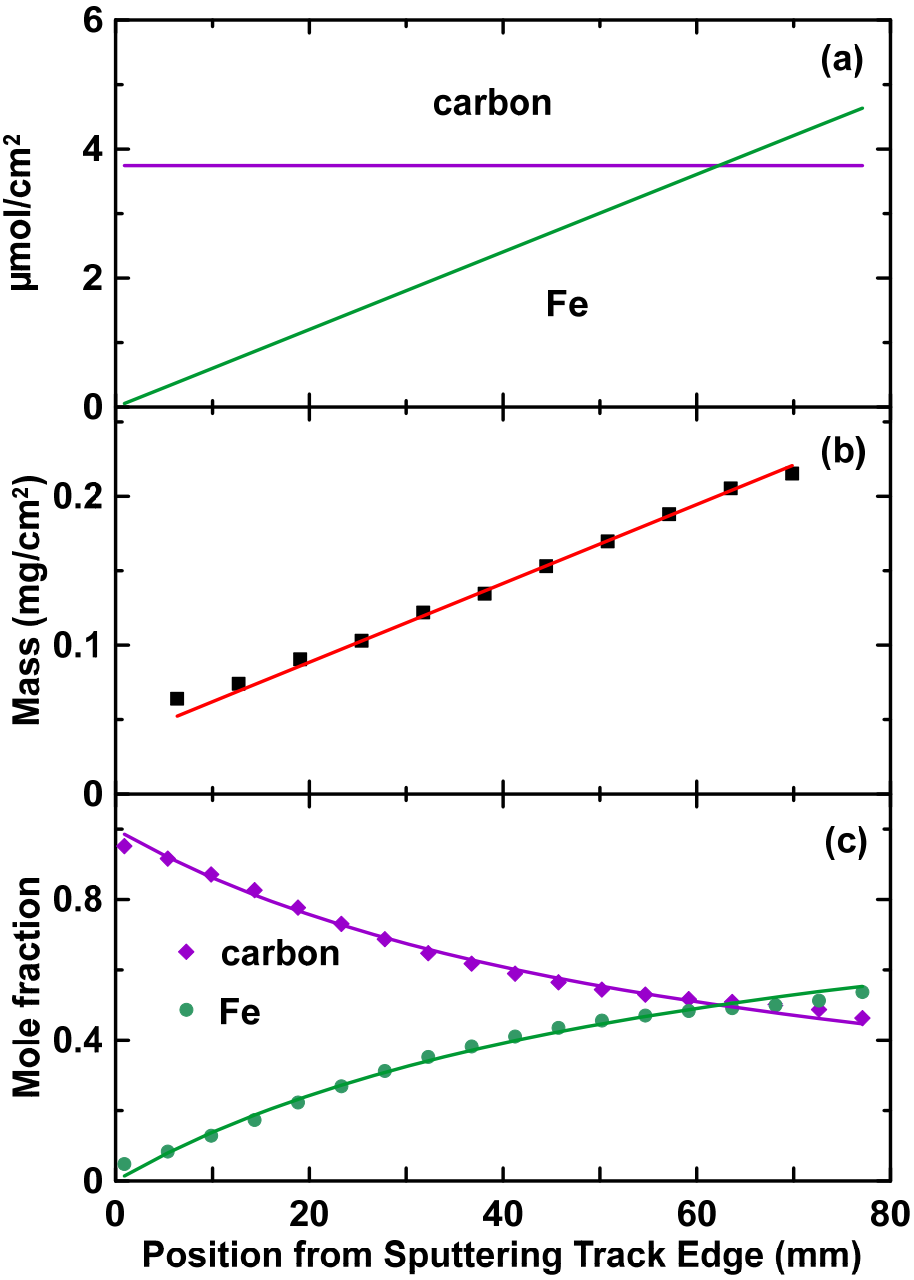
(a)
carbon
Fe
µmol/cm²
6
4
2
0
(b)
Mass (mg/cm²)
0.2
0.1
0
(c)
Mole fraction
carbon
Fe
0.8
0.4
0
0
20
40
60
80
Position from Sputtering Track Edge (mm)

Figure 2

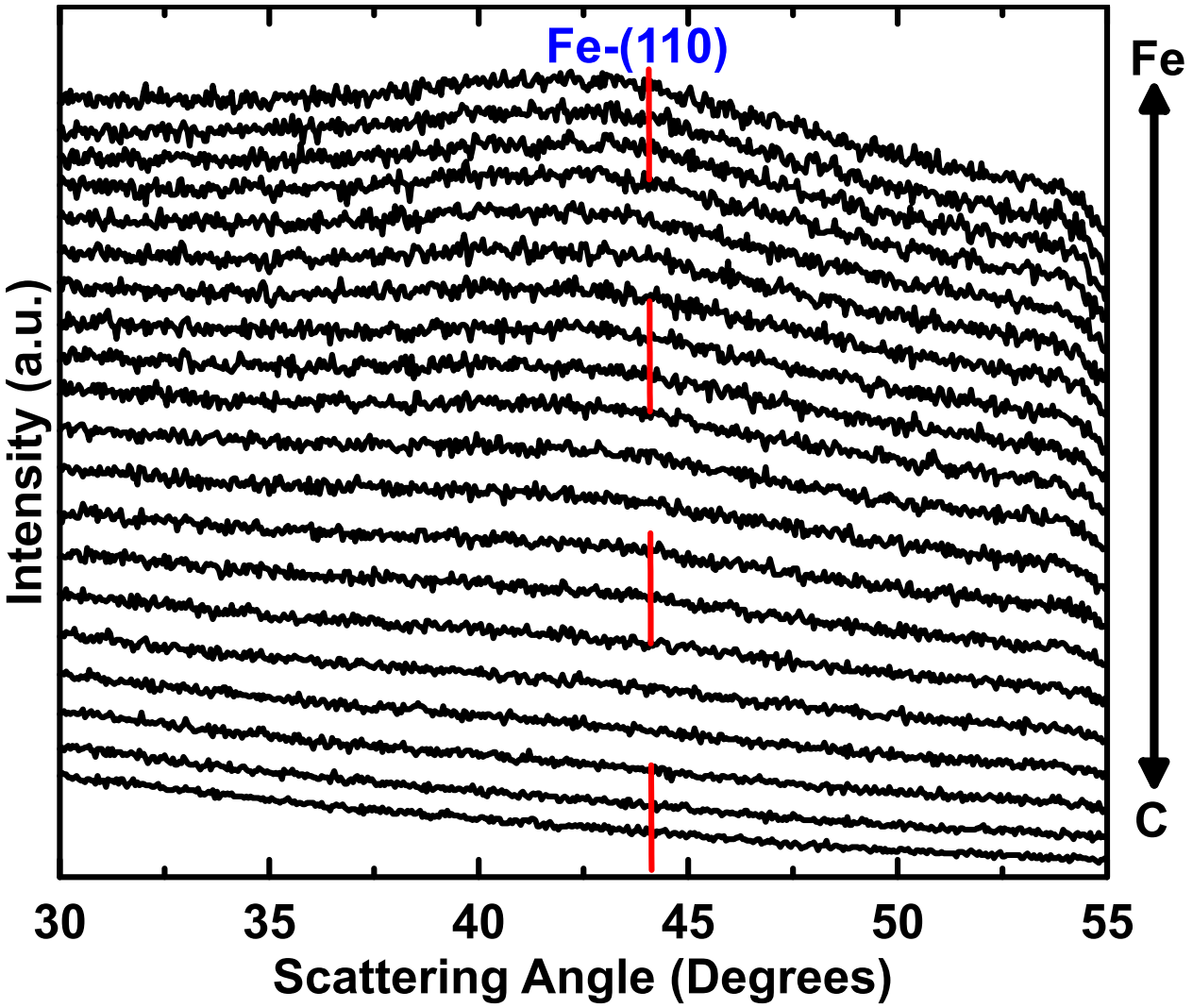
Fe-(110)
Fe
C
Intensity (a.u.)
30
35
40
45
50
55
Scattering Angle (Degrees)

Figure 3

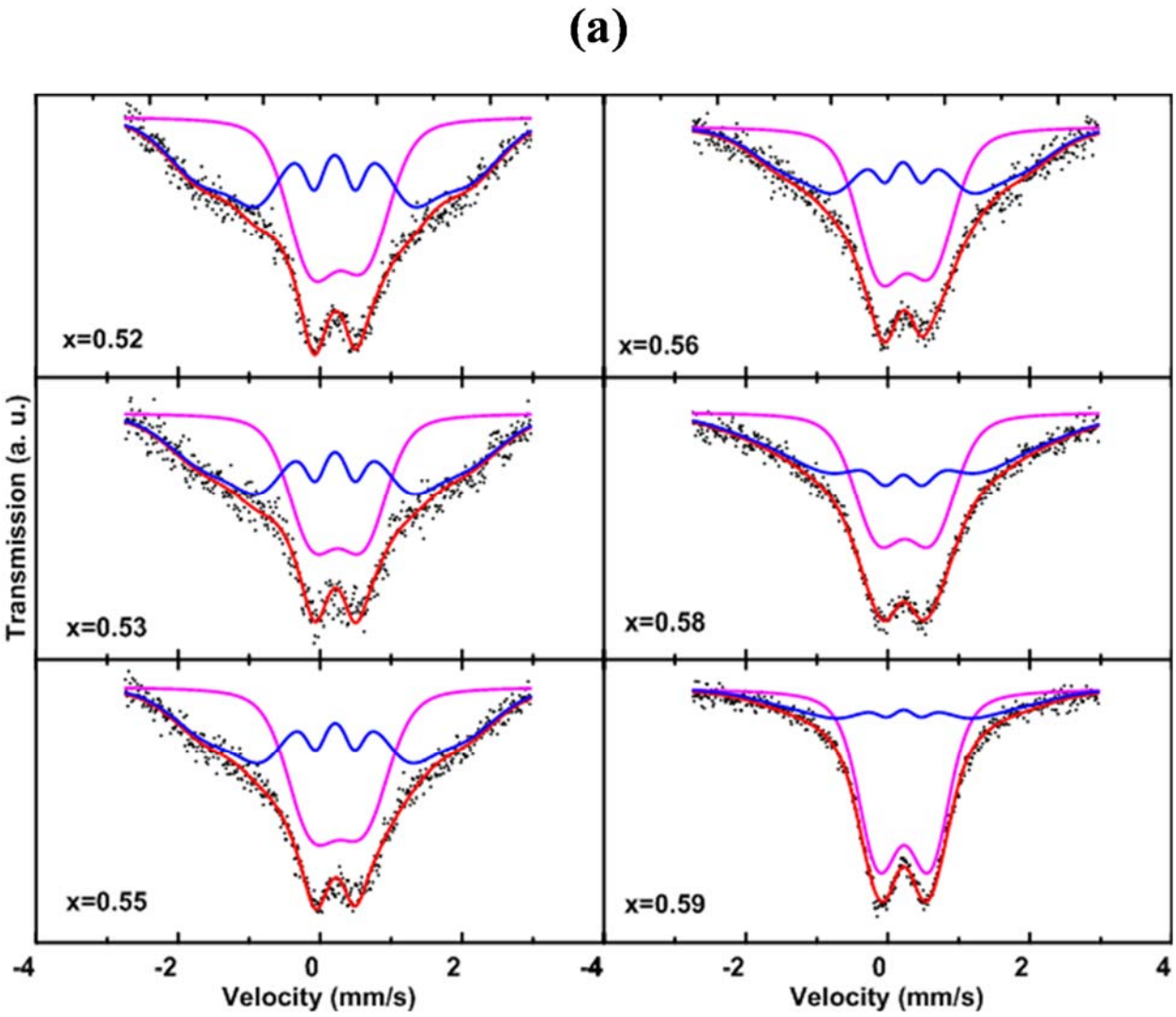
(a)
x=0.52
x=0.56
x=0.53
x=0.58
x=0.55
x=0.59
Transmission (a. u.)
-4
-2
0
2
-4
-2
0
2
4
Velocity (mm/s)
Velocity (mm/s)

**(b)**

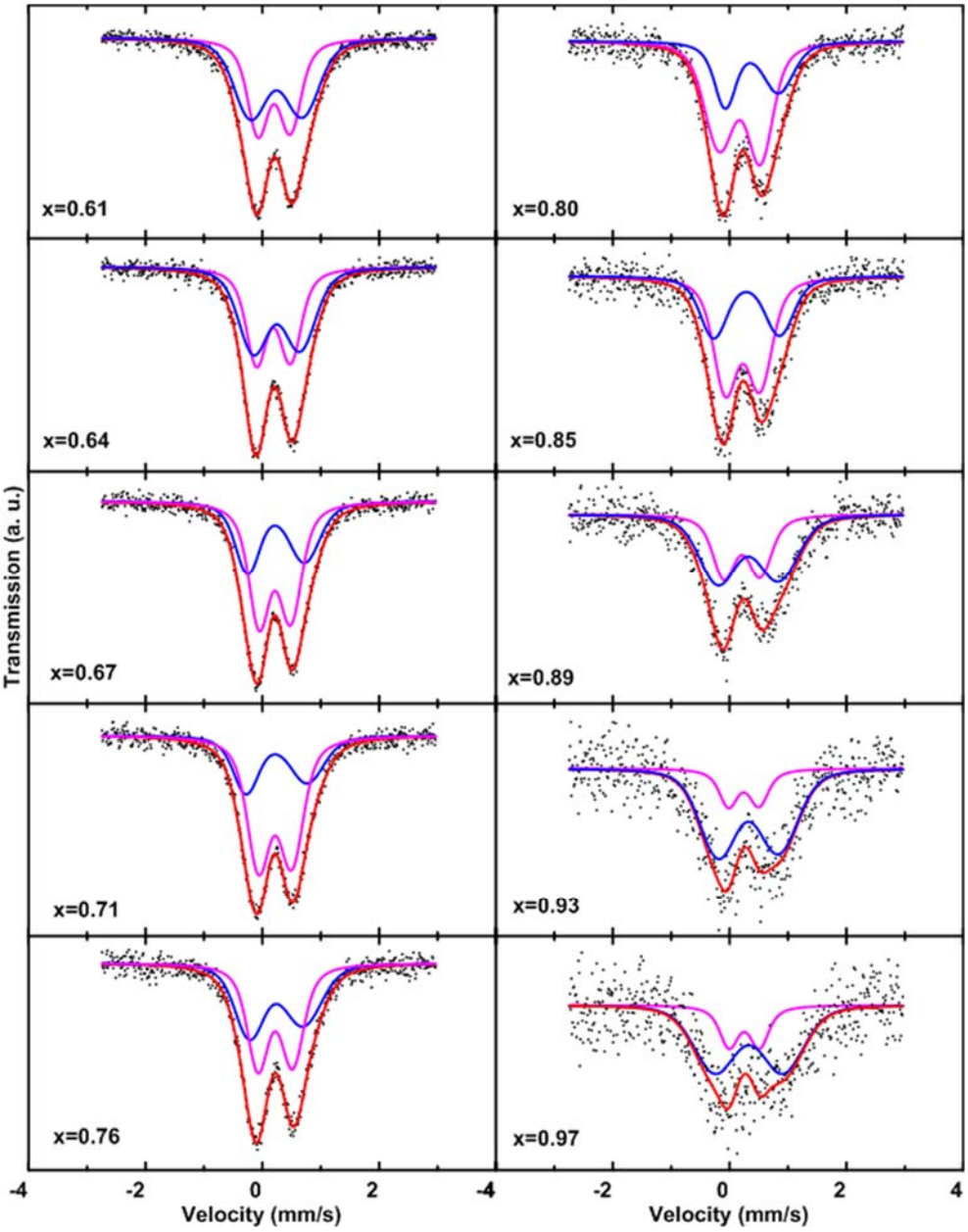
x=0.61
x=0.80
x=0.64
x=0.85
x=0.67
x=0.89
x=0.71
x=0.93
x=0.76
x=0.97
Transmission (a. u.)
Velocity (mm/s)
Velocity (mm/s)
-4
-2
0
2
-4
-2
0
2
4

Figure 4

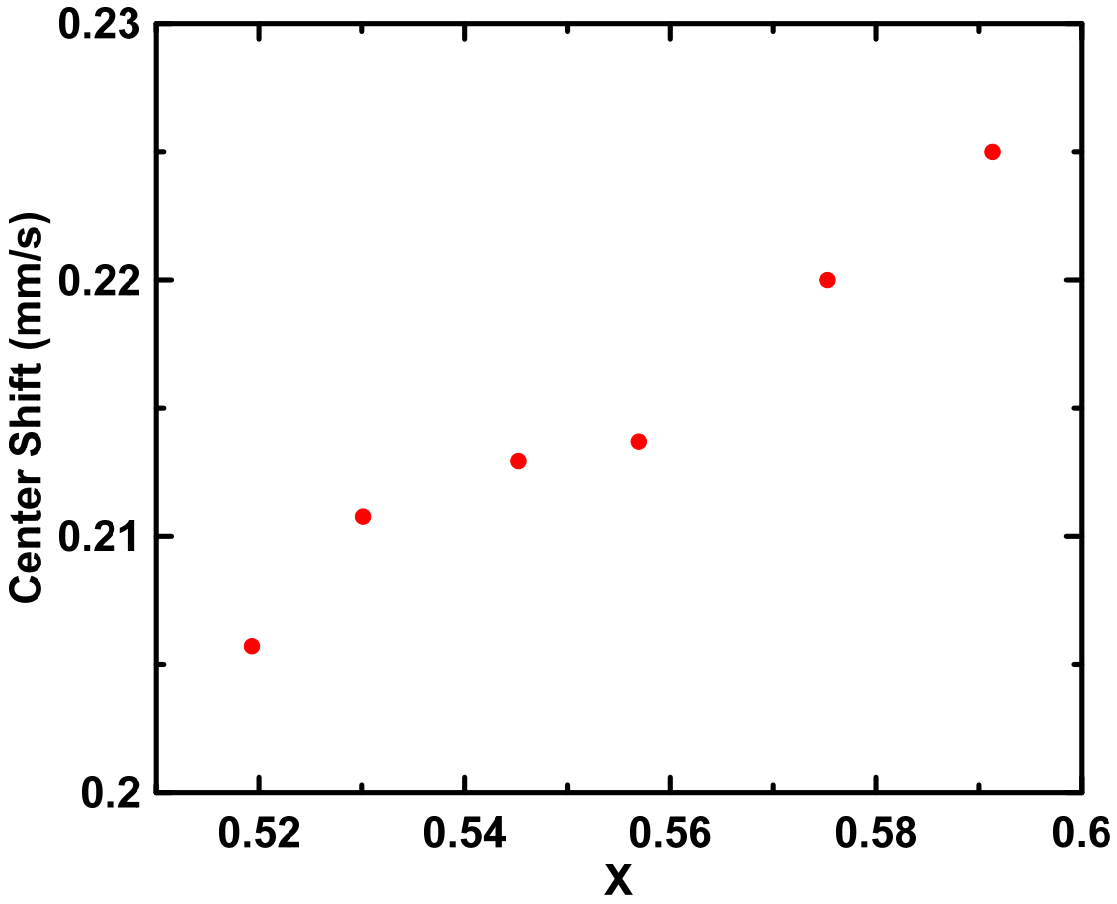


(a)

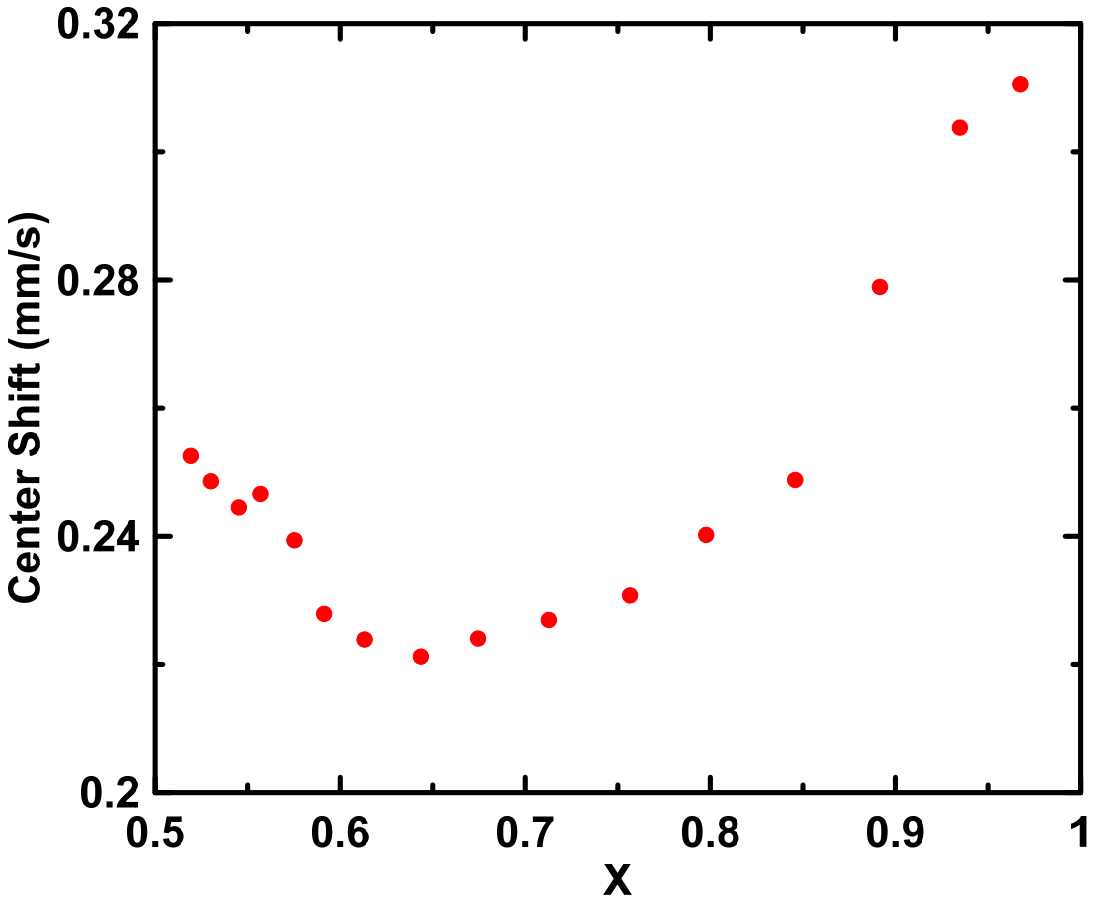


(b)

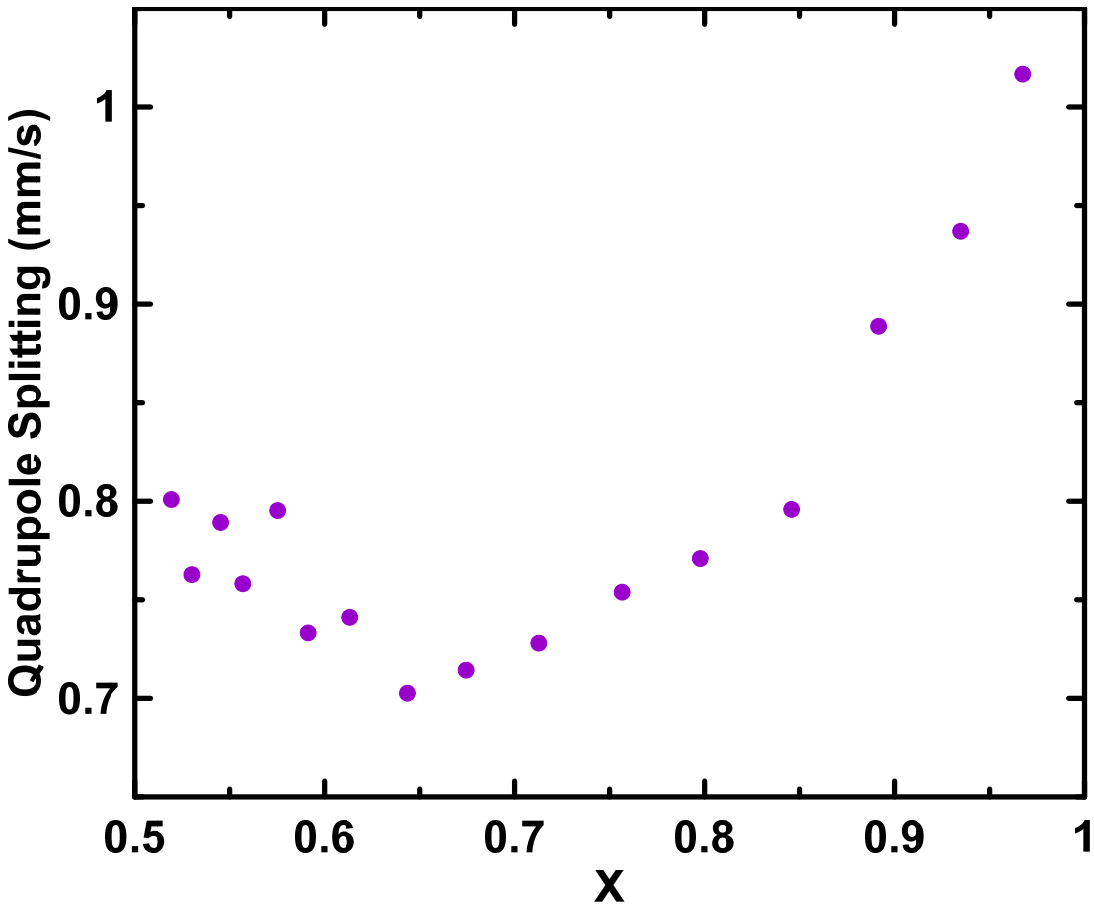


(c)

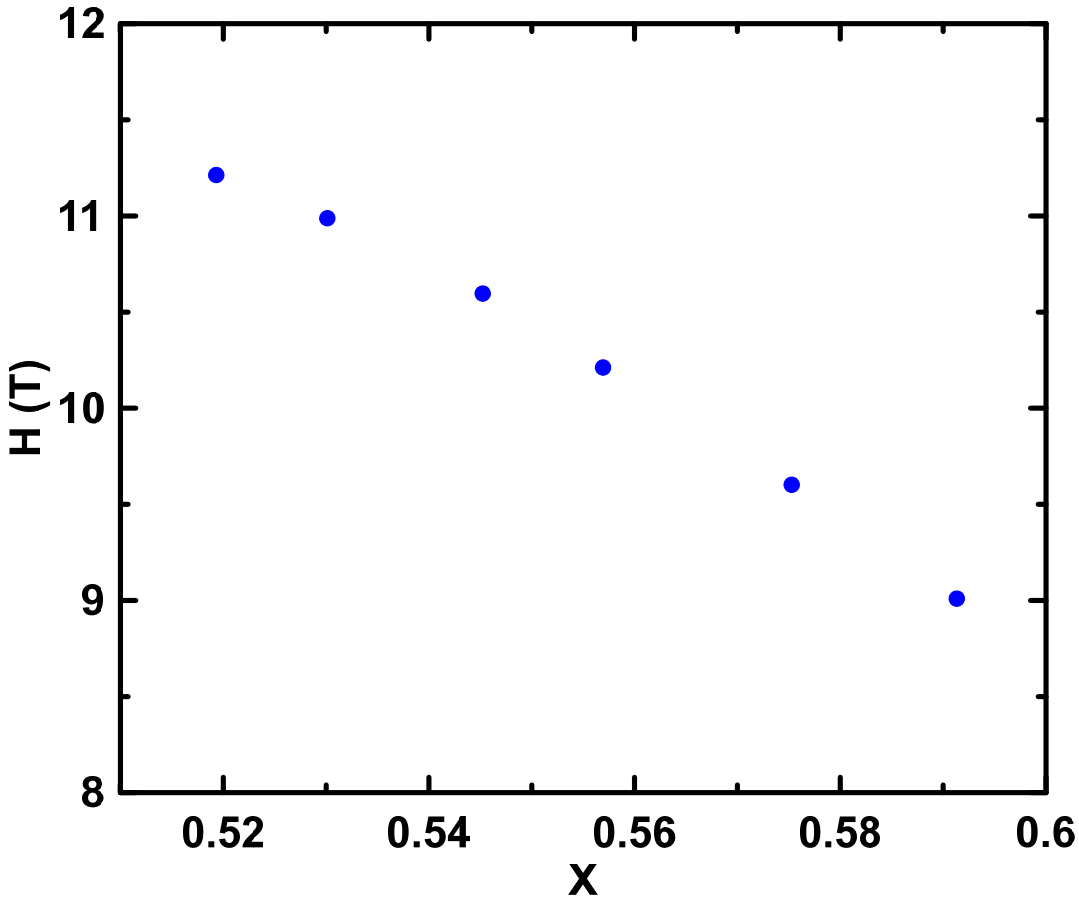


(d)

Figure 5

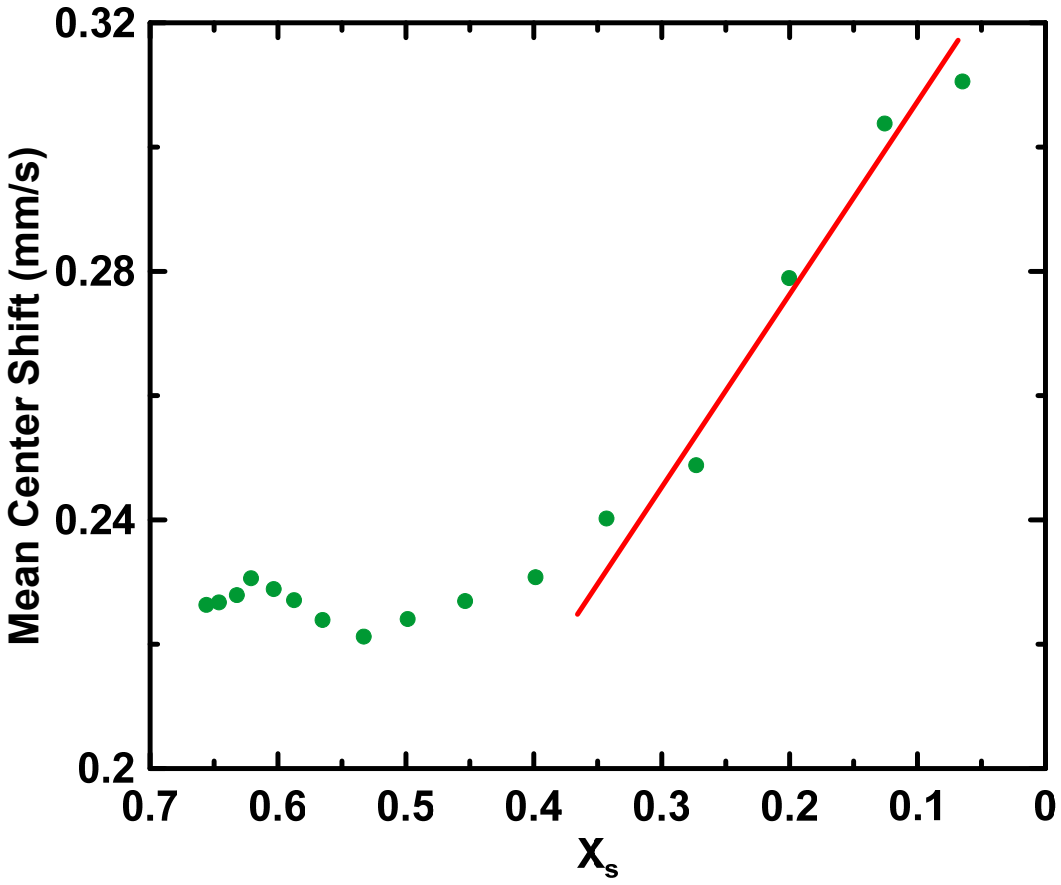

Figure 6

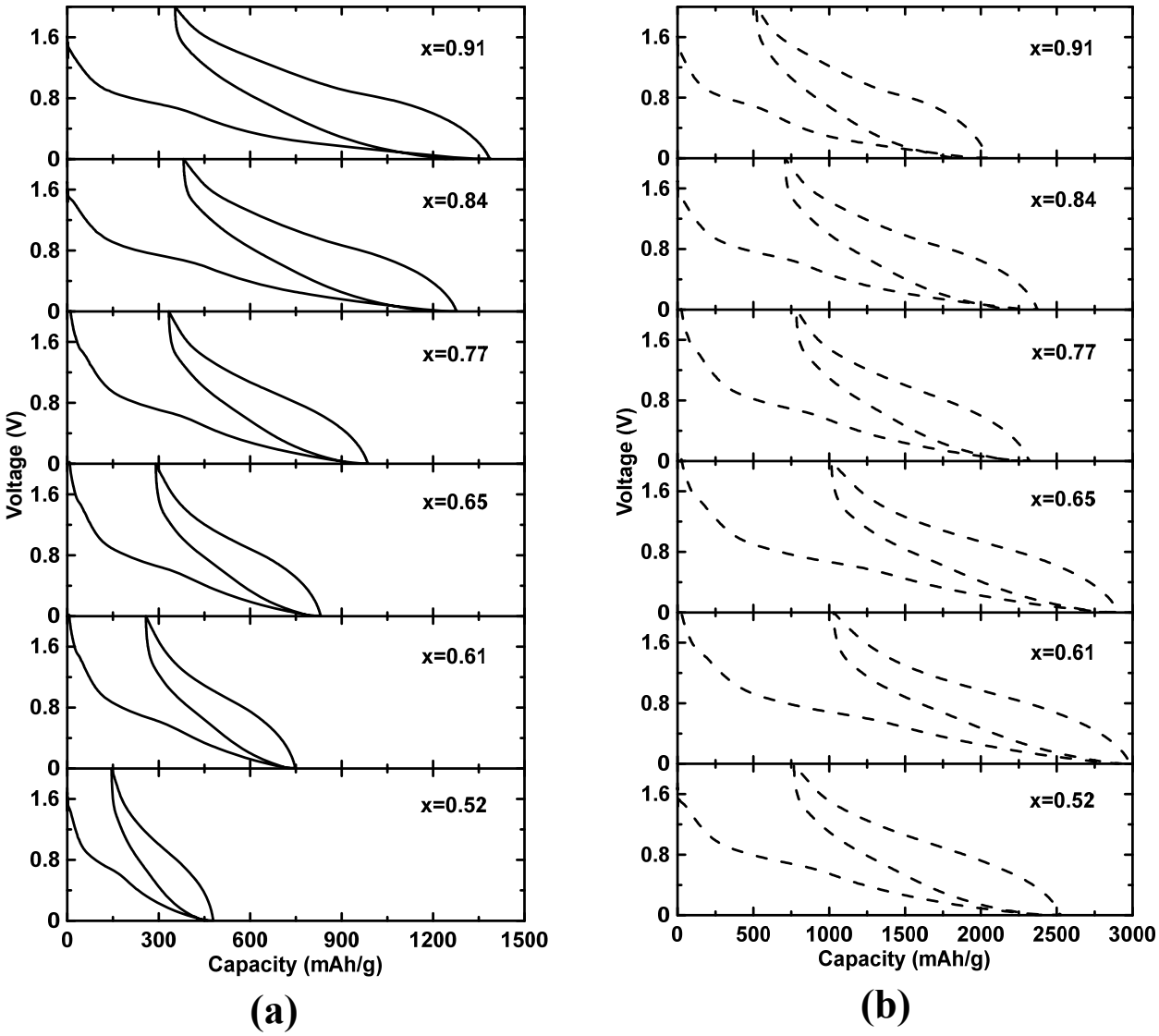
x=0.91
x=0.84
x=0.77
x=0.65
x=0.61
x=0.52
Voltage (V)
Capacity (mAh/g)
0
0.8
1.6
0
300
600
900
1200
1500
0
500
1000
1500
2000
2500
3000
(a)
(b)

Figure 7

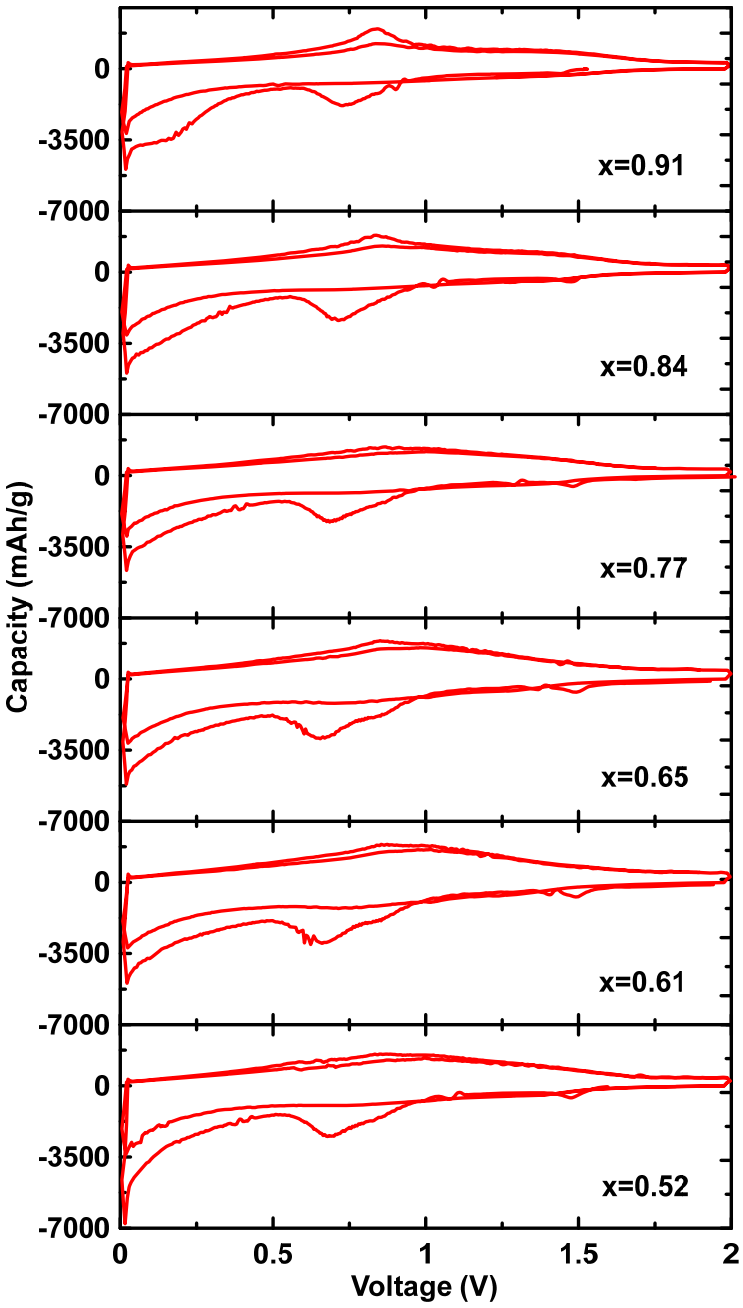
Capacity (mAh/g)
0
-3500
-7000
x=0.91
x=0.84
x=0.77
x=0.65
x=0.61
x=0.52
0
0.5
1
1.5
2
Voltage (V)

Figure 8

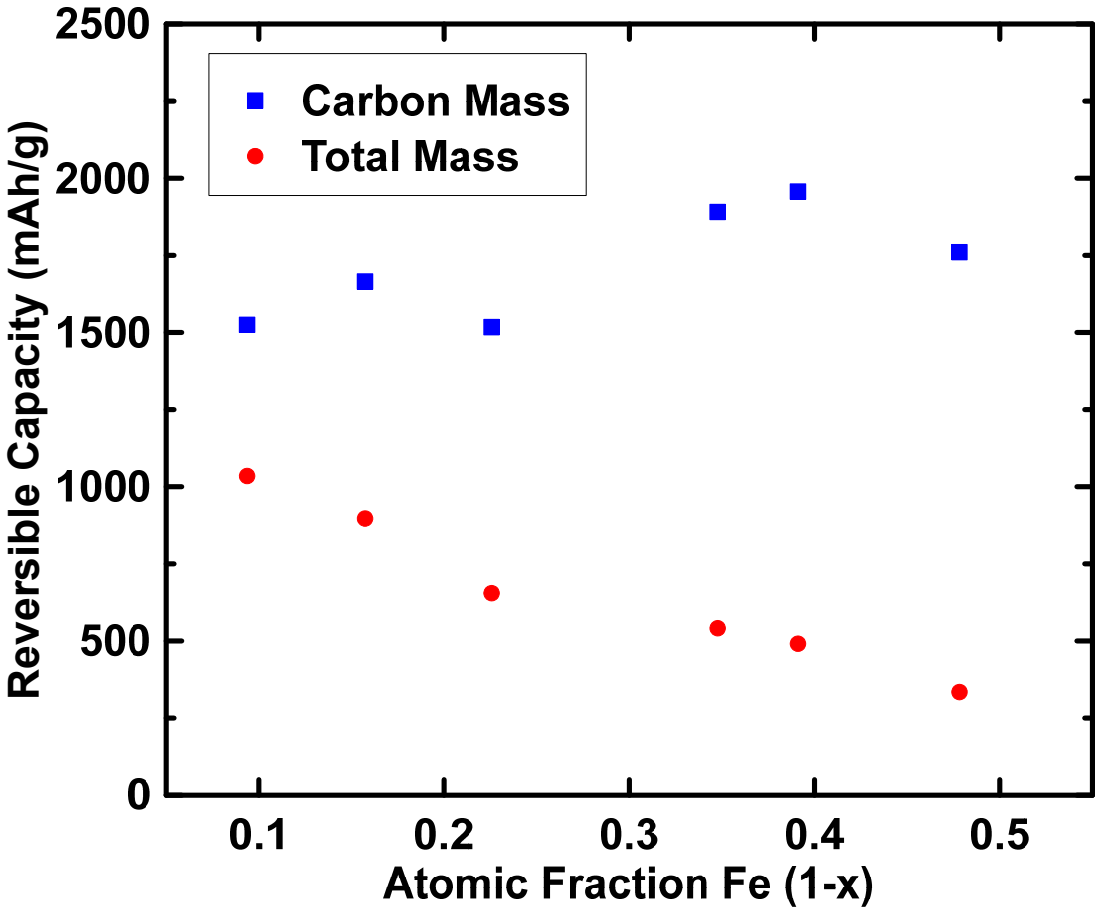
Carbon Mass
Total Mass
Reversible Capacity (mAh/g)
2500
2000
1500
1000
500
0
0.1
0.2
0.3
0.4
0.5
Atomic Fraction Fe (1-x)

Figure 9

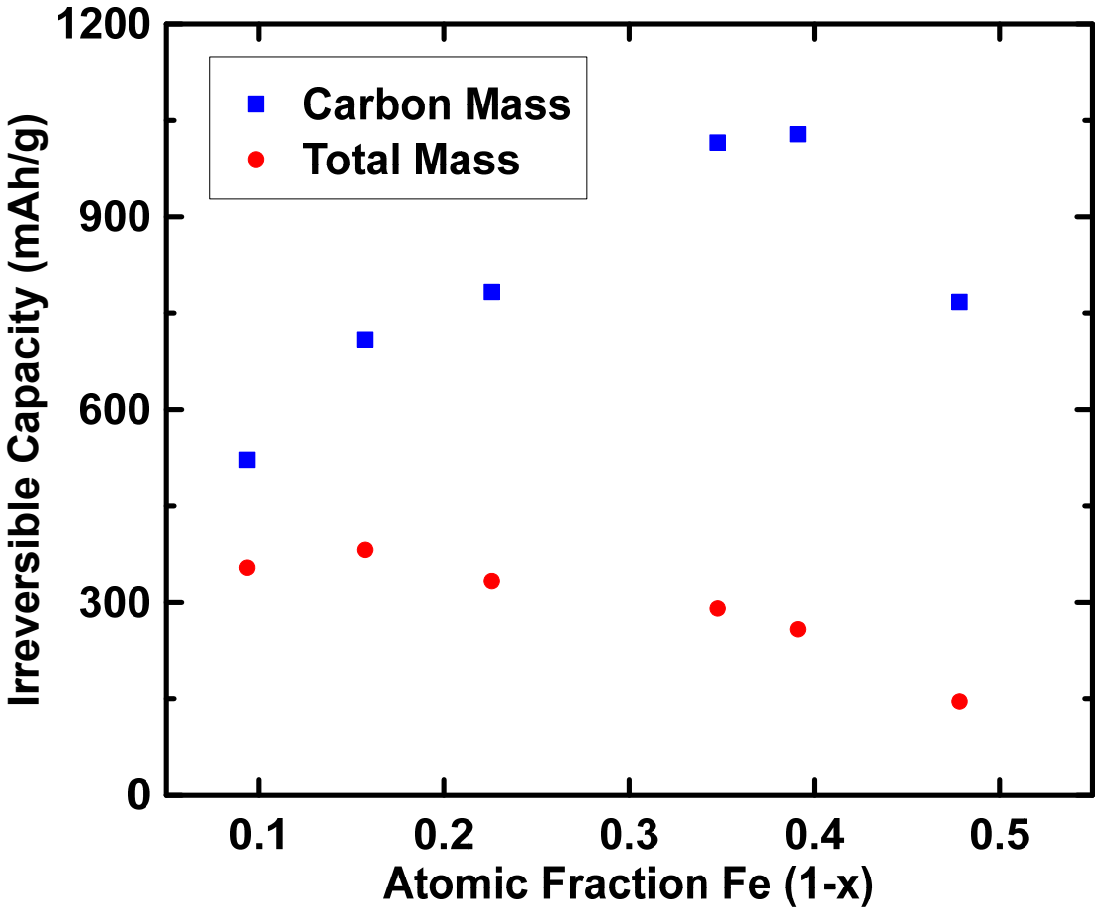
Carbon Mass
Total Mass
Irreversible Capacity (mAh/g)
1200
900
600
300
0
0.1
0.2
0.3
0.4
0.5
Atomic Fraction Fe (1-x)

Figure 10

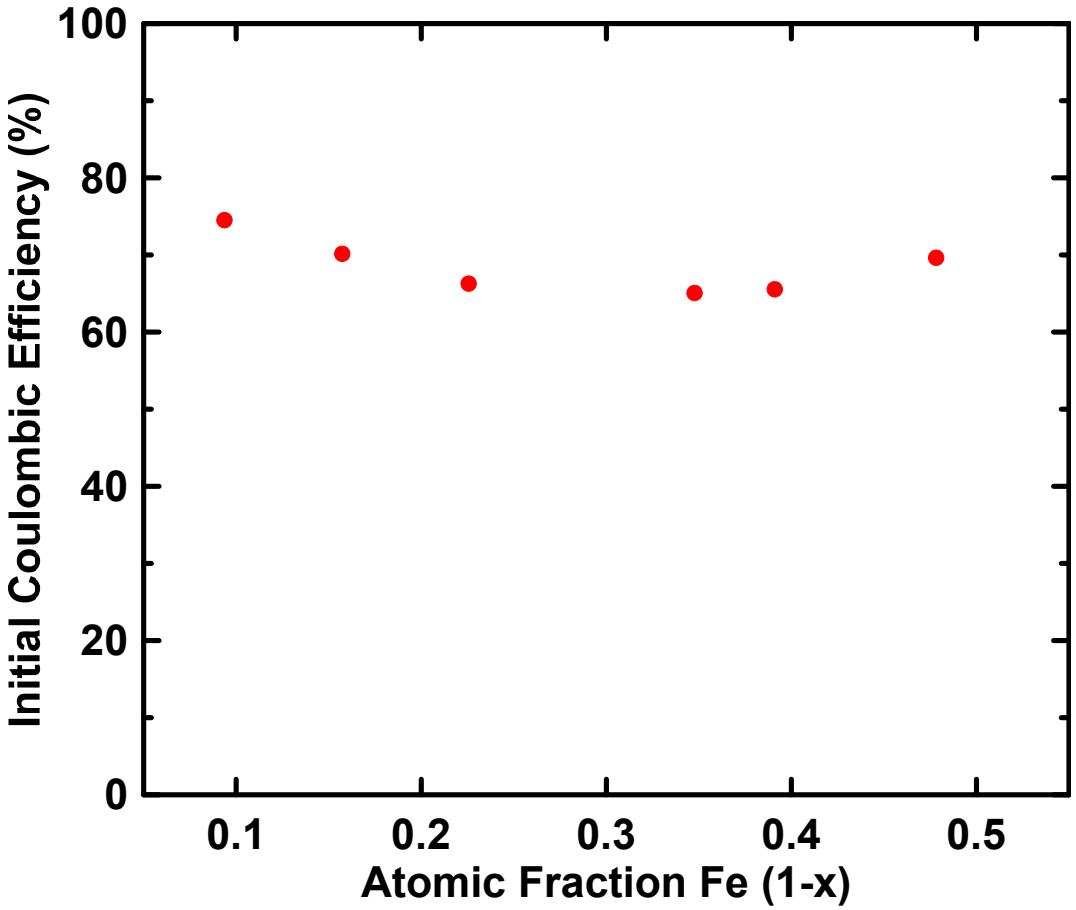
Initial Coulombic Efficiency (%)
100
80
60
40
20
0
0.1
0.2
0.3
0.4
0.5
Atomic Fraction Fe (1-x)